

Voltage switching and domain relocation in semiconductor superlattices

L. L. Bonilla[*], R. Escobedo and G. Dell'Acqua

*Grupo de Modelización y Simulación Numérica, Universidad Carlos III de Madrid,
Avenida de la Universidad 30, 28911 Leganés, Spain*

(Dated: February 5, 2020)

Abstract

A numerical study of domain wall relocation during voltage switching with different ramping times is presented for weakly coupled, doped semiconductor superlattices exhibiting multistable domain formation in the first plateau of their current-voltage characteristics. Stable self-oscillations of the current at the end of stable stationary branches of the current-voltage characteristics have been found. These oscillations are due to periodic motion of charge dipoles near the cathode that disappear inside the SL, before they can reach the receiving contact. Depending on the dc voltage step, the type of multistability between static branches and the duration of voltage switching, unusual relocation scenarios are found including changes of the current that follow adiabatically the stable I–V branches, different faster episodes involving charge tripoles and dipoles, and even small amplitude oscillations of the current near the end of static I–V branches followed by dipole-tripole scenarios.

PACS numbers: 73.63.-b, 05.45.-a, 73.23.-b, 73.40.-c

I. INTRODUCTION

Nonlinear vertical electron transport in semiconductor superlattices (SL) gives rise to a rich variety of dynamical phenomena associated with negative differential conductivity (NDC) [1, 2, 3, 4]. In wide miniband SL, NDC due to Bragg scattering is the origin of self-oscillations of the current through a dc voltage biased SL [5, 6]. These oscillations are due to recycling of charge dipoles as in the Gunn effect of bulk GaAs. In weakly coupled SL, NDC due to sequential tunneling between quantum wells may cause either stable self-sustained current oscillations mediated by traveling charge monopoles or dipoles [7, 8, 9], or a sawtooth multistable current–voltage (I–V) characteristics associated with static field domains [10, 11, 12]. The observed behavior depends crucially on the SL configuration (widths of wells and barriers, number of SL periods, boundary conditions in the contact regions), doping density and voltage bias [4].

Although there remain important gaps in our theoretical knowledge of nonlinear transport in SL [1, 4], a basic difference between weakly and strongly coupled SL is the type of balance equations describing them. Weakly coupled SL are described by spatially discrete balance equations whereas spatially continuous balance equations determine the nonlinear behavior of strongly coupled SL [2]. Traces of spatial discreteness are the sawtooth I–V characteristics and the current spikes during self-oscillations and during domain relocation due to voltage switching; see the review of theory and experiments in [4].

Recently, the dynamic response of the current and the field profile to voltage switching has been investigated both experimentally [13, 14, 15, 16, 17] and theoretically [18, 19]. For a SL with a multistable I–V characteristics, each branch thereof corresponds to having the domain wall separating the low and high field domains of the field profile (which is a charge accumulation layer, CAL) placed at a different well of the SL. We are interested in the transition from one stable stationary branch of the I–V characteristics to another due to a step in the applied voltage $\Delta V = V_f - V_i$ (V_i and V_f are the initial and final voltage values). Bias steps are turned on during a short time interval called *ramping time*, which can be zero. A bias step increasing the applied dc voltage is referred to as an *up jump* ($\Delta V > 0$), while a bias step decreasing the applied dc voltage is called a *down jump* ($\Delta V < 0$). Bias steps contrast with voltage up-sweeps and down-sweeps for which the ramping time is infinitely long and the bias increase or decrease is adiabatic. For down jumps, the relocation process

of the domain boundary proceeds via a direct motion of the CAL in the direction of electron flow. This behavior is confirmed by single-shot time traces of the current response: for values of V_f away from regions of bistability, there is an initial displacement current spike, after which the current rapidly switches to the stable value. Furthermore, when V_f is near to the bistable region, there is an additional intermediate period, in which the current fluctuates about a metastable value for a stochastically varying delay time τ_d , before rapidly switching to the stable value in a time τ_s [14, 15]. However, for up jumps, the charge monopole at the domain boundary would have to move against the electron flow, and this is only possible for small-amplitude up jumps. For larger up jumps, the more complex dipole-tripole scenario occurs: the CAL moves one well against the electron flow, then a charge dipole comprising one CAL and one charge depletion layer (CDL) is formed at the cathode and, together with the old CAL, it moves with the electron flow. The resulting charge tripole exists until the old CAL reaches the anode and disappears, leaving only the charge dipole. The CDL of this dipole reaches the anode while its CAL moves until its final position at the destination branch of the I–V characteristics [16, 18]. For V_f near the end of a branch, there are pronounced stochastic effects due to shot noise [15, 17].

In this paper, we carry out an extensive numerical study of the dynamical response to voltage switching and unveil unexpected behavior. We use a discrete sequential tunneling model whose detailed description can be found in Appendix A of [2]. Stochastic effects due to shot noise will be ignored. We find stable self-oscillations of the current at the end of stable stationary branches of the I–V characteristics. These oscillations are due to periodic motion of charge dipoles near the cathode that disappear inside the SL, before they can reach the receiving contact. We also want to understand how the dynamical response to voltage switching is affected by the number of multistable branches of the I–V characteristics, their extension and the *ramping time* necessary to change voltage (from V_i to V_f). Among our results, we find a different tripole-dipole scenario than that reported by Amann et al [18] (the first phase of the scenario is different). We also find that the ramping time selects the tripole–dipole scenario for large up jumps. Suppose that there are several branches of the I–V characteristics in the interval between V_i and V_f (large voltage switching). Then there are two critical ramping times τ_{c1} and τ_{c2} , $\tau_{c2} < \tau_{c1}$, whose precise values depend on the SL parameters in Table I and on V_i and V_f . For the parameters used in our simulations, the critical ramping times are between 10 and 30 μs . If the ramping time is larger than

τ_{c1} , the current follows adiabatically the stable branches until their end, falls to the next stable branch and repeats this process until V_f is reached. For ramping times between τ_{c2} and τ_{c1} , adiabatic motion over a stable branch is followed by a tripole–dipole scenario until the following stable branch is reached. Depending on the number of multistable branches, sometimes a stable branch is skipped in this process. Lastly, if the ramping time is shorter than τ_{c2} , the final stable branch is reached after only one tripole–dipole scenario even for large voltage steps.

The rest of the paper is as follows. The model we use and details of its numerical integration are described in Sections II and III, respectively. Section IV contains the multistable I–V characteristics of a SL with realistic configuration and doping density parameters [8]. We show that the width of the multistability regions increases with voltage while the slope of the branches (which is the positive differential conductivity or, in short, PDC) decreases. These features affect substantially the dynamic response to switching described in Sections V and VI. Finally, the main results of the paper are summarized in Section VII.

II. SEQUENTIAL TUNNELING DISCRETE MODEL

In weakly coupled SL, typically the scattering times (about 0.1 ps) are much shorter than the escape times from quantum wells (about 0.01 ns for a SL with a 0.1 meV miniband width). In their turn, the latter are shorter than typical dielectric relaxation times (on the nanosecond time scale) [4]. This implies that the dominant mechanism of vertical charge transport is sequential resonant tunneling and that the tunneling current across barriers can be considered to be stationary on the time scale of dielectric relaxation. Nonlinear stationary and oscillatory phenomena occurring for voltages in the first plateau of weakly coupled doped SL have been well described by the spatially discrete model equations (with backward finite differences) introduced in [20] with constitutive relations between sequential tunneling current, electron densities and electric field of the type calculated in [21] using stationary nonequilibrium Green functions or in [2] (and references cited therein) approximating Transfer Hamiltonian formulas. See the review [4] for a recent description and further justification. The model equations consist of the Poisson and charge continuity equations for the two-dimensional (2D) electron density n_i and average electric field $-F_i$ at the i th SL period (which starts at the right end of the $(i - 1)$ th barrier and finishes at the right end of

the i th barrier)

$$F_i - F_{i-1} = \frac{e}{\varepsilon}(n_i - N_D), \quad (1)$$

$$\frac{dn_i}{dt} = J_{i-1 \rightarrow i} - J_{i \rightarrow i+1}, \quad i = 1, \dots, N. \quad (2)$$

Here N_D , ε , $-e$ and $eJ_{i \rightarrow i+1}$ are the 2D doping density at the i th well, the average permittivity, the electron charge and the tunnelling current density across the i th barrier, respectively. The width of a SL period is $l = d + w$, where d and w are the barrier and well widths, respectively. Time-differencing Eq. (1) and inserting the result in Eq. (2), we obtain the following form of Ampere's law,

$$\varepsilon \frac{dF_i}{dt} + J_{i \rightarrow i+1} = J(t), \quad (3)$$

which may be solved with the bias condition for the applied voltage $V(t)$:

$$\frac{1}{N+1} \sum_{i=0}^N F_i = \frac{V(t)}{(N+1)l}. \quad (4)$$

The space-independent unknown function $J(t)$ is the total current density through the SL. The $2N + 2$ independent equations of the discrete model are (1) for $i = 1, \dots, N$, (3) for $i = 0, \dots, N$ and (4) for the $2N + 2$ unknowns n_i , F_i ($i = 1, \dots, N$), F_0 and J , provided we have $N + 1$ constitutive relations linking the tunneling current $J_{i \rightarrow i+1}$ ($i = 0, \dots, N$) to the electron densities and electric fields. To calculate the tunneling currents across SL barriers, we use explicit formulas provided by the Transfer Hamiltonian method when the scattering broadening is much smaller than the subband energies and chemical potentials [2]:

$$J_{i \rightarrow i+1} = \frac{e v^{(f)}(F_i)}{l} \left\{ n_i - \frac{m^* k_B T}{\pi \hbar^2} \ln \left[1 + \exp \left(-\frac{e F_i l}{k_B T} \right) \right] \right. \\ \left. \times \left(\exp \left(\frac{\pi \hbar^2 n_{i+1}}{m^* k_B T} \right) - 1 \right) \right\}, \quad i = 1, \dots, N-1, \quad (5)$$

$$J_{0 \rightarrow 1} = \sigma F_0, \quad (6)$$

$$J_{N \rightarrow N+1} = \sigma F_N \frac{n_N}{N_D}. \quad (7)$$

As boundary tunneling currents for $i = 0$ and N , we adopt linear relations between current and field as in Ref. [18]. In these formulas, σ is the contact conductivity (assumed to be the same at both contacts for simplicity), m^* the effective mass, T the temperature, k_B and \hbar are the Boltzmann and Planck constants respectively, and the ‘‘forward tunneling velocity’’

$v^{(f)}$ is a sum of Lorentzians centered at the resonant field values $F_{C\nu} = (\mathcal{E}_{C\nu} - \mathcal{E}_{C1})/(el)$:

$$v^{(f)}(F_i) = \sum_{j=1}^n \frac{\frac{\hbar^{3l}(\gamma_{C1} + \gamma_{C_j})}{2m^{*2}} \mathcal{T}_i(\mathcal{E}_{C1})}{(\mathcal{E}_{C1} - \mathcal{E}_{C_j} + eF_i l)^2 + (\gamma_{C1} + \gamma_{C_j})^2}, \quad (8)$$

$$\mathcal{T}_i(\epsilon) = \frac{16k_i^2 k_{i+1}^2 \alpha_i^2 (k_i^2 + \alpha_i^2)^{-1} (k_{i+1}^2 + \alpha_i^2)^{-1}}{(w + \alpha_{i-1}^{-1} + \alpha_i^{-1})(w + \alpha_{i+1}^{-1} + \alpha_i^{-1}) e^{2\alpha_i d}}, \quad (9)$$

$$\hbar k_i = \sqrt{2m^* \epsilon}, \quad (10)$$

$$\hbar k_{i+1} = \sqrt{2m^* [\epsilon + e(d+w)F_i]}, \quad (11)$$

$$\hbar \alpha_{i-1} = \sqrt{2m^* \left[eV_b + e \left(d + \frac{w}{2} \right) F_i - \epsilon \right]}, \quad (12)$$

$$\hbar \alpha_i = \sqrt{2m^* \left[eV_b - \frac{ewF_i}{2} - \epsilon \right]}, \quad (13)$$

$$\hbar \alpha_{i+1} = \sqrt{2m^* \left[eV_b - e \left(d + \frac{3w}{2} \right) F_i - \epsilon \right]}. \quad (14)$$

In these equations, C_j indicates the j th subband in a well, \mathcal{E}_{C_j} is its energy measured from the bottom of the well, γ_{C_j} is the scattering width, \mathcal{T}_i is a dimensionless transmission probability across the i th barrier, and eV_b is the barrier height in absence of potential drops. Typical values of these parameters are shown in Table I.

TABLE I: Parameters of the 9/4 SL in Ref [8].

N	N_D	d_W/d_B	γ	m^*	\mathcal{E}_{C_1}	\mathcal{E}_{C_2}	\mathcal{E}_{C_3}	V_b
	(cm^{-2})	(nm/nm)	(meV)	(10^{-32} Kg)	(meV)	(meV)	(meV)	(V)
40	1.5×10^{11}	9.0/4.0	8	8.43	44	180	410	0.982

To carry out numerical integrations of the discrete model, the explicit formulas (5) - (14) are much better than numerically calculated tunneling currents such as those obtained in [1, 21] from Green function calculations. Furthermore, explicit tunneling currents are better suited for analysis of the discrete model equations. These reasons to favor the previous explicit formulas for the sequential tunneling current are not offset by claims that one type of derivation (Transfer Hamiltonian or Green functions) agrees better with first principles: both derivations involve similarly drastic simplifications and the resulting formulas agree similarly well with experiments. It turns out that the type of solutions of the discrete model depends on the *qualitative features* of $J_{i \rightarrow i+1}$ as a function of F_i , n_i and n_{i+1} , not on detailed

quantitative features. The formulas for $J_{i \rightarrow i+1}$ obtained using different derivation methods yield a tunneling current similar to that in Fig. 1, which is why we obtain similar results. See discussions in Ref. [4].

III. NONDIMENSIONALIZATION AND NUMERICAL INTEGRATION

For numerical treatment, it is convenient to render the equations dimensionless. We have used the following definitions [4]

$$\begin{aligned} \mathcal{F}_i &= \frac{F_i}{F_M}, \quad \tilde{n}_i = \frac{n_i}{N_D}, \quad \mathcal{J}_{i \rightarrow i+1} = \frac{J_{i \rightarrow i+1}}{J_M}, \quad \mathcal{J} = \frac{J}{J_M}, \quad \tilde{t} = \frac{t}{t_0} \equiv \frac{J_M t}{\varepsilon F_M}, \\ v(\mathcal{F}_i) &= \frac{v^{(f)}(F_i)}{v_M}, \quad \phi = \frac{V}{V_0} \equiv \frac{V}{(N+1)F_M l}, \quad \tilde{\sigma} = \rho_c \sigma \equiv \frac{F_M \sigma}{J_M}, \quad v_M = \frac{J_M l}{e N_D}. \end{aligned} \quad (15)$$

The values F_M and J_M are defined as the field and current density at which the tunneling current $J_{i \rightarrow i+1}$ of (5) reaches its first relative maximum, provided $n_i = n_{i+1} = N_D$. With these definitions, the model equations are

$$\frac{d\mathcal{F}_i}{d\tilde{t}} + \mathcal{J}_{i \rightarrow i+1} = \mathcal{J}, \quad i = 0, \dots, N, \quad (16)$$

$$\tilde{n}_i = \frac{\mathcal{F}_i - \mathcal{F}_{i-1}}{\nu} + 1, \quad i = 1, \dots, N, \quad (17)$$

$$\sum_{i=0}^N \mathcal{F}_i = (N+1)\phi(t), \quad t \geq 0, \quad (18)$$

$$\mathcal{J}_{i \rightarrow i+1} = v(\mathcal{F}_i) \left\{ \tilde{n}_i - \rho_0 \ln \left[1 + e^{-a\mathcal{F}_i} \left(e^{\frac{\tilde{n}_{i+1}}{\rho_0}} - 1 \right) \right] \right\}, \quad i = 1, \dots, N-1, \quad (19)$$

$$\mathcal{J}_{0 \rightarrow 1} = \tilde{\sigma} \mathcal{F}_0, \quad (20)$$

$$\mathcal{J}_{N \rightarrow N+1} = \tilde{\sigma} \mathcal{F}_N \tilde{n}_N, \quad (21)$$

where

$$\nu = \frac{e N_D}{\varepsilon F_M}, \quad \rho_0 = \frac{m^* k_B T}{\pi \hbar^2 N_D}, \quad a = \frac{e l F_M}{k_B T}, \quad (22)$$

are dimensionless parameters. Their values for the SL described in Table I are given in Table II. Figure 1 shows the tunneling current density as a function of a homogeneous field profile $F_i = F$ when the electron densities are set equal to the doping density in all the SL wells. We observe several relative maxima, the first of which yields the values of F_M and J_M . The field intervals between two consecutive maxima roughly correspond to plateaus in the I-V characteristics.

TABLE II: Typical scales for $T = 5$ K.

F_M	J_M	v_M	x_0	t_0	ν	ρ_0	ρ_c	V_0
(kV/cm)	(A/cm ²)	(m/s)	(nm)	(ns)	(-)	(-)	(Ω m)	(V)
-	-	$\frac{J_M l}{e N_D}$	$\frac{\varepsilon F_M l}{e N_D}$	$\frac{\varepsilon F_M}{J_M}$	$\frac{e N_D}{\varepsilon F_M}$	$\frac{m^* k_B T}{\pi \hbar^2 N_D}$	$\frac{l F_M}{e v_M N_D}$	$F_M N l$
3.945	3.127	1.691	2.494	2.066	5.212	0.111	12.62	0.205

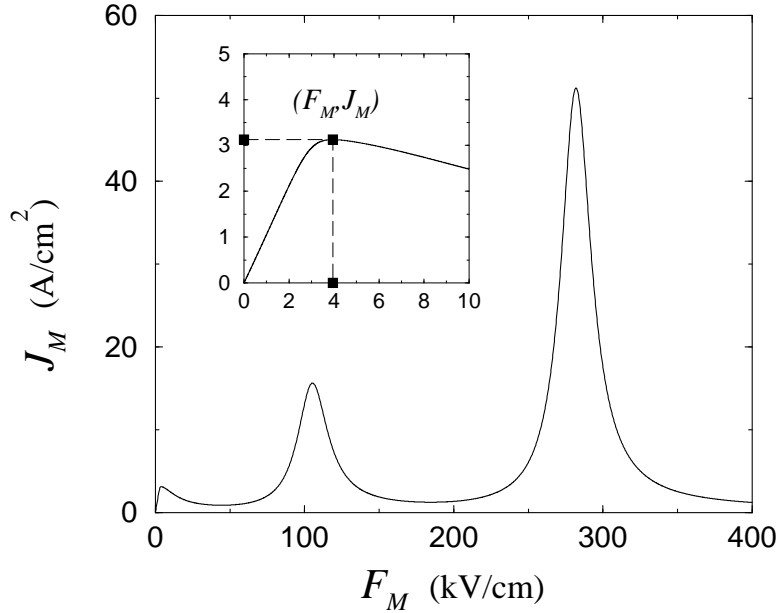


FIG. 1: Tunneling current density for $n_i = n_{i+1} = N_D$ as a function of field $F_i = F$, showing that $F_M \approx 3.945$ kV/cm and $J_M \approx 3.1269$ A/cm² for $T = 5$ K and the SL values of Table I.

In order to numerically solve the discrete model, we first sum (16) from $i = 0$ to N and use the bias condition (18) to calculate \mathcal{J} . The result is

$$\mathcal{J} = \frac{d\phi(t)}{dt} + \frac{1}{N+1} \sum_{i=0}^N \mathcal{J}_{i \rightarrow i+1}. \quad (23)$$

To solve (16)-(21) together with the initial condition

$$\mathcal{F}_i(0) = \mathcal{F}_{i0}, \quad i = 0, \dots, N, \quad \phi(0) = \sum_{i=0}^N \frac{\mathcal{F}_{i0}}{N+1}, \quad (24)$$

is equivalent to solving (17) - (21) plus the following equation instead of (16):

$$\frac{d\mathcal{F}_i}{d\tilde{t}} = \frac{d\phi}{d\tilde{t}} + \frac{1}{N+1} \sum_{j=0, j \neq i}^N \mathcal{J}_{j \rightarrow j+1} - \frac{N}{N+1} \mathcal{J}_{i \rightarrow i+1}, \quad i = 0, \dots, N. \quad (25)$$

The new system of equations also satisfies the bias condition (18). This can be checked by adding all equations (25) from $i = 0$ to N which implies that $\sum_{i=0}^N \mathcal{F}_i - (N+1)\phi$ is a constant, equal to zero because of the initial conditions. To solve our dimensionless equations, we have used an embedded Runge-Kutta method of order 7(8) with step-size control and error estimate, checking the results independently by means of an implicit BDF (backward differentiation formula) method of order 1 to 4, solved by means of Newton-Raphson iterations. These methods are more accurate than those used by Amann et al [18].

IV. I-V CHARACTERISTICS

We have constructed numerically the first plateau of the I-V characteristics of the SL whose parameters are compiled in Table I at a temperature of 5K and a contact resistivity $1/\sigma = 25.2 \Omega\text{m}$ ($\tilde{\sigma} = 0.5$). We depict in Fig. 2 the portion of the stable static branches obtained by voltage up-sweep from zero volts to the end of the first plateau and also the portion obtained by voltage down-sweep from high voltage values. Note that the upper parts of odd numbered branches (from the 23rd to the 33rd) do not appear because they correspond to regions of bistability and are skipped during voltage up-sweep. Likewise, the central parts of branches 35th to 39th are not shown because they correspond to regions of tristability and are skipped during voltage up-sweep and down-sweep. All these curves can be entirely shown by up-sweeping starting from the parts thereof shown in the figure. The voltage distribution for different locations of the domain boundary for a fixed applied voltage in regions of multistability is shown in Figures 8 and 9 of the review paper [4], which contains further background discussions and references to pertinent literature. The basin of attraction of the static branches shown in Fig. 2 is very small near their ends and it is mainly in these regions that our high precision numerical methods make the difference with previous calculations; see Fig. 3. We have found that the I-V branches may undergo Hopf bifurcations to small-amplitude oscillatory solutions near their upper ends, as we explain in Section VI.

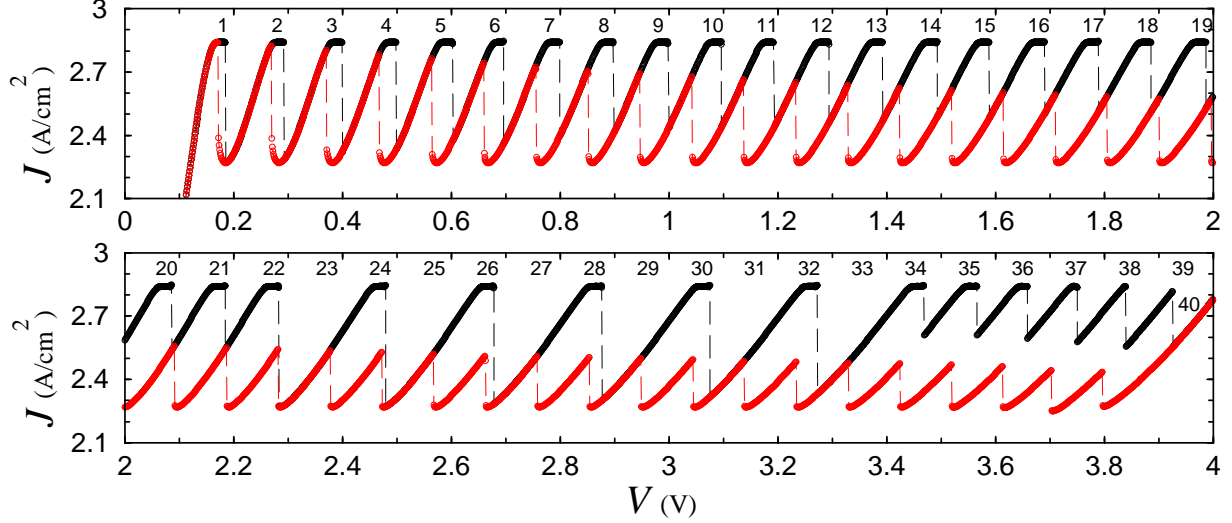


FIG. 2: (Color online) I–V characteristics of the 40-period 9-4 SL of Ref. [8] obtained by up- and down-sweeping adiabatic processes for $V \in [0, 4]$ V. Parameters correspond to Table I at 5K and with cathode resistivity of $25.2 \Omega\text{m}$ ($\tilde{\sigma} = 0.5$). The branch number increases with voltage: the i th branch has a CAL separating low and high field domains which is located at the $(N - i + 1)$ th well.

According to their stability feature, we can distinguish four different types of I–V branch:

1. The first branch B_1 is singly stable from $V = 0$ until its upper part coincides with the lower end of branch B_2 , giving rise to a narrow region of bistability.
2. From branch B_2 to B_{21} , we observe that the branch length increases (the extension of B_2 is 0.122 V whereas that of B_{19} is 0.177 V) while their slope (the PDC) decreases. We see that the low voltage branches have a steep slope similar to that below the first maximum of the homogeneous tunneling current density in Fig. 1, whereas the high voltage branches have a smaller slope similar to that of the low part of the ascent to the second maximum in Fig. 1. Why? The field profile in the low voltage branches is similar to that of a solution with spatially uniform field, which therefore obeys $J_{i \rightarrow i+1}(F, N_D, N_D) = J$, thereby corresponding to the first branch of the curve in Fig. 1. Similarly, high voltage branches are close to spatially homogeneous field profiles satisfying the same relation, but now the field profile corresponds to the third branch of Fig. 1. Branches with intermediate voltages are a combination of low and high field domains, and therefore their slopes are interpolations between low and high PDC. The central part of each branch is singly stable, while their two ends are bistable. As the

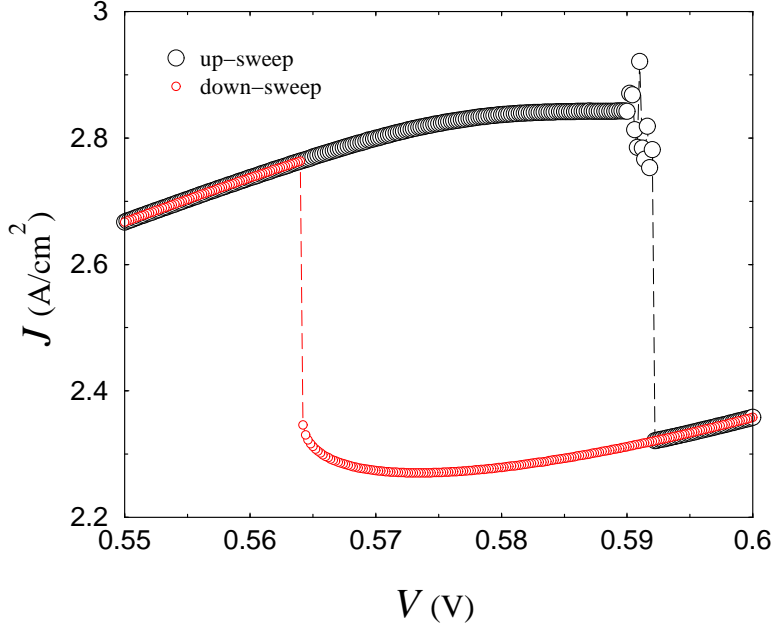


FIG. 3: (Color online) Bistability between Branches 5 and 6 of the I–V characteristics in Fig. 2 ($V \in [0.55, 0.6]$ V). The stationary solution becomes unstable to a small-amplitude oscillatory solution at the upper end of Branch 5.

branch number increases, the central part shrinks and the bistable regions including the ends of the branch grow.

3. Branch B_{22} is the last one having a central singly stable region and the first one with a tristability region near its upper end. In the tristability region, branch B_{22} coexists with the central part of branch B_{23} and the lower part of branch B_{24} .
4. Branch B_{23} is bistable except in its central part and its upper end where it is tristable. The lower part of this branch is still bistable.
5. Branches B_{24} to B_{39} are tristable in their central parts and ends, but they have two bistability regions. As voltage increases, the tristability regions grow at the expense of the bistability regions.
6. The last branch of the first plateau, B_{40} , has a tristable lower end, a bistable central region and it is singly stable from there until it reaches the second plateau in its upper end.

V. LARGE SWITCHING: EVOLUTION OF $J(V)$ ALONG THE I - V CURVE

In this Section, we describe the dynamical response of the SL to a voltage switching $V(t) = V_i + \Delta V t H(\tau_r - t)/\tau_r + \Delta V H(t - \tau_r)$, in which ΔV is constant, and $H(t) = 1$ if $t > 0$, $H(t) = 0$ if $t < 0$ is the Heaviside unit step function. We select the initial voltage in the central part of one branch and the final voltage $V_f = V_i + \Delta V$ in different parts of another stable branch, so that several branches can be found between V_i and V_f . We have found different scenarios.

A. Switching from bistable branches: modified tripole-dipole scenario

Let us choose $V_i = 0.83\text{V}$, in the central singly stable part of branch B_8 and $V_f = 1.37\text{V}$, on the central part of branch B_{14} . These branches are bistable but they have a central part for whose voltages no other static solution is stable (the branch is singly stable there). Fig. 4 shows the dynamical response of the total current density $J(t)$ to voltage switching with two different ramping times. For large enough ramping times (not shown), the current density $J(t)$ follows adiabatically the I - V characteristics. Below a first critical value of the ramping time, $J(t)$ cannot reach the upper end of the branches and it falls to the lower part of the following branch in the voltage range where both branches are stable. *For each branch crossing*, this fall occurs via the following modified tripole-dipole scenario whose current trace is depicted in Fig. 5:

- Phase 1 The CAL separating low and high field domains stay in the same well while the current density increases until it surpasses the critical value at which $J = \sigma F$ intersects the curve in Fig. 1, $J = J_{i \rightarrow i+1}(F, N_D, N_D)$ on the second branch thereof ($J_c \approx 2.9 \text{ A/cm}^2$).
- Phase 2 A charge dipole wave is created at the cathode and it starts moving to the anode while the old CAL also moves towards the anode. After a short transient during which the current decreases, the whole structure, a *charge tripole* moves rigidly towards the anode.
- Phase 3 The old CAL reaches the anode leaving a charge dipole moving (after a short transient during which the current further decreases) rigidly towards the anode at a lower speed than the tripole.

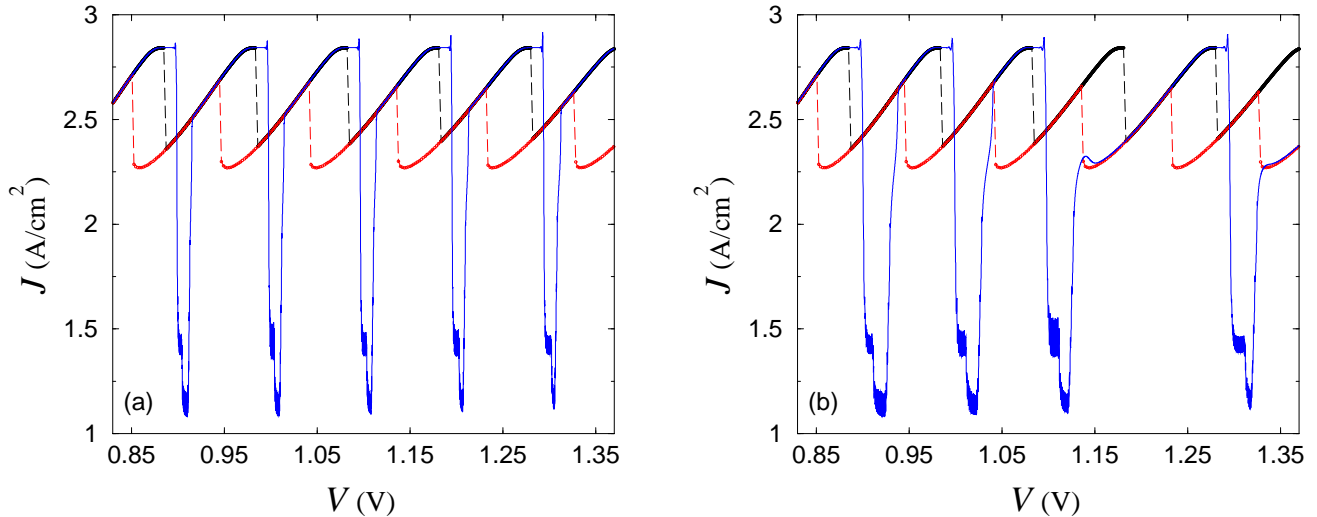


FIG. 4: (Color online) Total current density during voltage switching from $V_i = 0.83\text{V}$ to $V_f = 1.37\text{V}$ (seven branches) for ramping times: (a) $\tau_r = 30\mu\text{s}$ (dimensionless value: $\tilde{\tau}_r = 2 \times 10^4$), and (b) $\tau_r = 15\mu\text{s}$ ($\tilde{\tau}_r = 10^4$). Thick black line: upper part of the I-V branches, red thin line: lower part of the static I-V branches, thin blue line: response curve ($V(t), J(t)$). In (a), the current follows adiabatically the I-V curve, whereas in (b), the ramping time is so short that the 4th and 6th branches are skipped. The dimensionless cathode conductivity is $\tilde{\sigma} = 0.5$.

Phase 4 The front part of the dipole, a CDL, reaches the anode leaving only the CAL in its back part. The current density increases to higher values corresponding to the next stable static solution while the CAL moves towards its final destination separating low and high field domains of the stable static field profile.

Phase 2 is characterized by double-peaked current spikes (corresponding to the well-to-well jumps of the two CAL) while Phases 3 and 4 exhibit single current spikes; see Fig. 5. Phases 2, 3 and 4 are exactly as described in [18] (who did not describe Phase 4) and corrected in [16] (who added Phase 4). In these previous works, Phase 1 was characterized by a one-well motion of the CAL towards the cathode. Note that experimental observations refer only to the behavior of the current density, not to the motion of domain walls, and therefore they cannot discriminate between our Phase 1 and the different one reported in [18]. To explain the differences in Phase 1, we note that, according to Fig. 3 of Ref. [22], a CAL may move against the electron flow if the current is large enough and the doping density is sufficiently large. However, the critical current for this motion would be exponentially

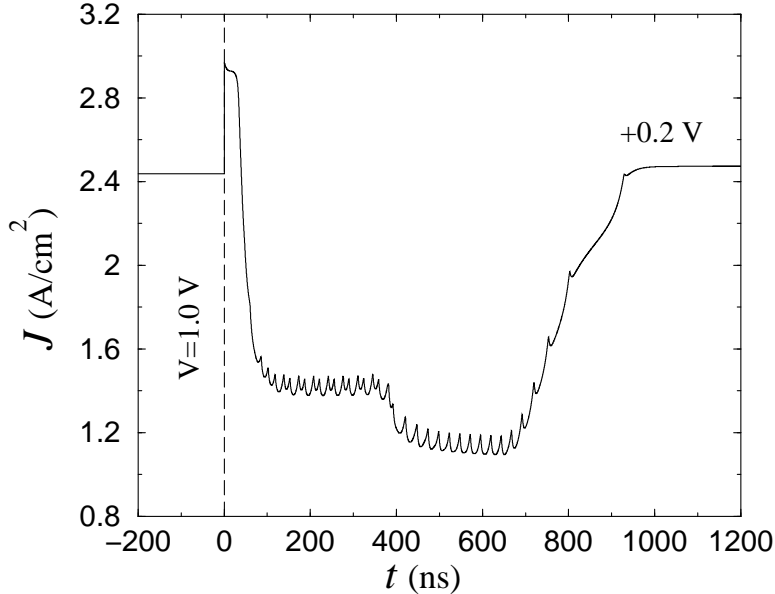


FIG. 5: Time trace of the total current density $J(t)$ after sudden voltage switching characterizing the tripole-dipole scenario. Here $V_i = 1.0$ V (for $t < 0$) and $\Delta V = 0.2$ V.

close to the maximum current for which CAL exist if the doping density is even larger, thereby eliminating in practice the possibility for CAL to move against the electron flow under current bias. In the simulations by Amann et al, the interval of currents allowing CAL motion against the electron flow was relatively wide (cf. their Figure 4), whereas we found that it was negligible for the tunneling current and doping density used in the present calculations. Then the increase of voltage due to switching is compensated by simply a current increase in Phase 1, without CAL motion, as indicated in Fig. 5. When the current surpasses its critical value (see the current spike over the maximum current value for static branches in Fig. 4), Phase 2 begins: a dipole is shed from the cathode and it moves on towards the anode together with the old CAL. This and subsequent Phases are as in the previous works [15, 18]. The behavior of the current can be explained using singular perturbation ideas as described in the reviews [2, 4]. Since the final position of the CAL approaches the cathode as the voltage increases, the dipole trip becomes shorter as shown in Fig. 4.

We have seen that switching from B_8 to B_{14} occurs by a succession of tripole-dipole scenarios. What happens if we continue decreasing the ramping time? It turns out that we start skipping branches. Note that the tripole-dipole process is quite fast in Fig. 4(a) and

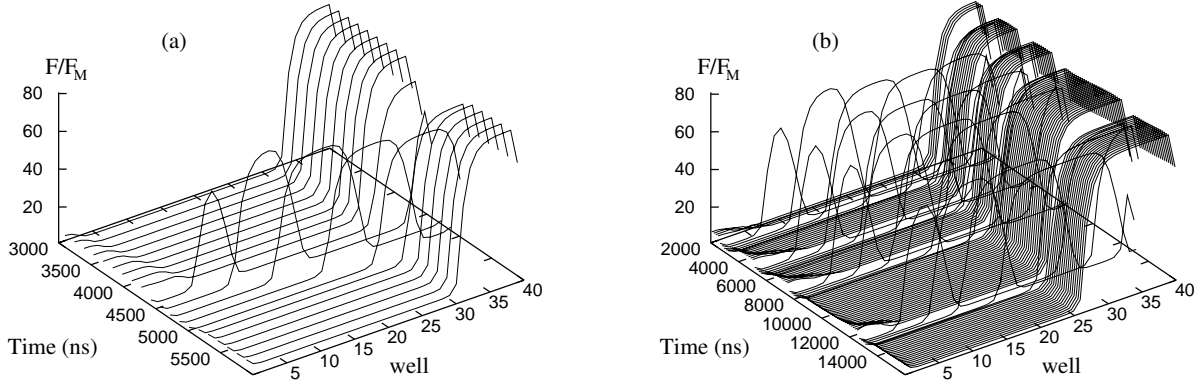


FIG. 6: Field profiles corresponding to Fig. 4 during relocation of the domain wall. (a) Detail of the emission and the travel of the CAL during the second relocation stage in Fig. 4(a). (b) The 4th branch in Fig. 4(b) has been skipped, therefore the 4th CAL is missing and there is no relocation stage.

it ends at a voltage smaller than the bistability interval near the end of the corresponding I-V branch. At that voltage, only one branch is stable and $J(t)$ follows this static branch until the next dipole emission. However, recall that the bistability intervals grow at the expense of the singly stable central part of the branches as their voltage increases. When the ramping time is decreased below a critical value (which depends on the branch), the voltage at the end of a process of dipole emission and travel may be in the bistability range of two branches. The CAL of the dipole then stops at the position corresponding to the static branch with lower current which is closer to the cathode than the CAL of the branch with higher current. This is observed in Fig. 4(b). Note that the branches B_{11} and B_{13} have been skipped. Fig. 6(b) shows that the corresponding tripole-dipole process is longer when one branch has been skipped.

B. Same switching range for bistable and tristable branches

It should be clear from the previous discussion that the intervals of bistability have great influence on the dynamic response to voltage switching. To make this clearer, we have depicted in Figures 7(a) to (h) the dynamic response to a voltage switching of width $\Delta V = 0.5$ V with ramping time $\tau_r = 30\mu\text{s}$ (as in Fig. 4(a)) for different initial voltages

V_i . We observe that the tripole-dipole scenario occurs for small V_i , branches start to be skipped as V_i increases, and the tripole-dipole process disappears at even larger voltages at which the tristability range of the branches is very large. Of course, the occurrence of the tripole-dipole scenario depends on the ramping time: it reappears again as the ramping time decreases sufficiently.

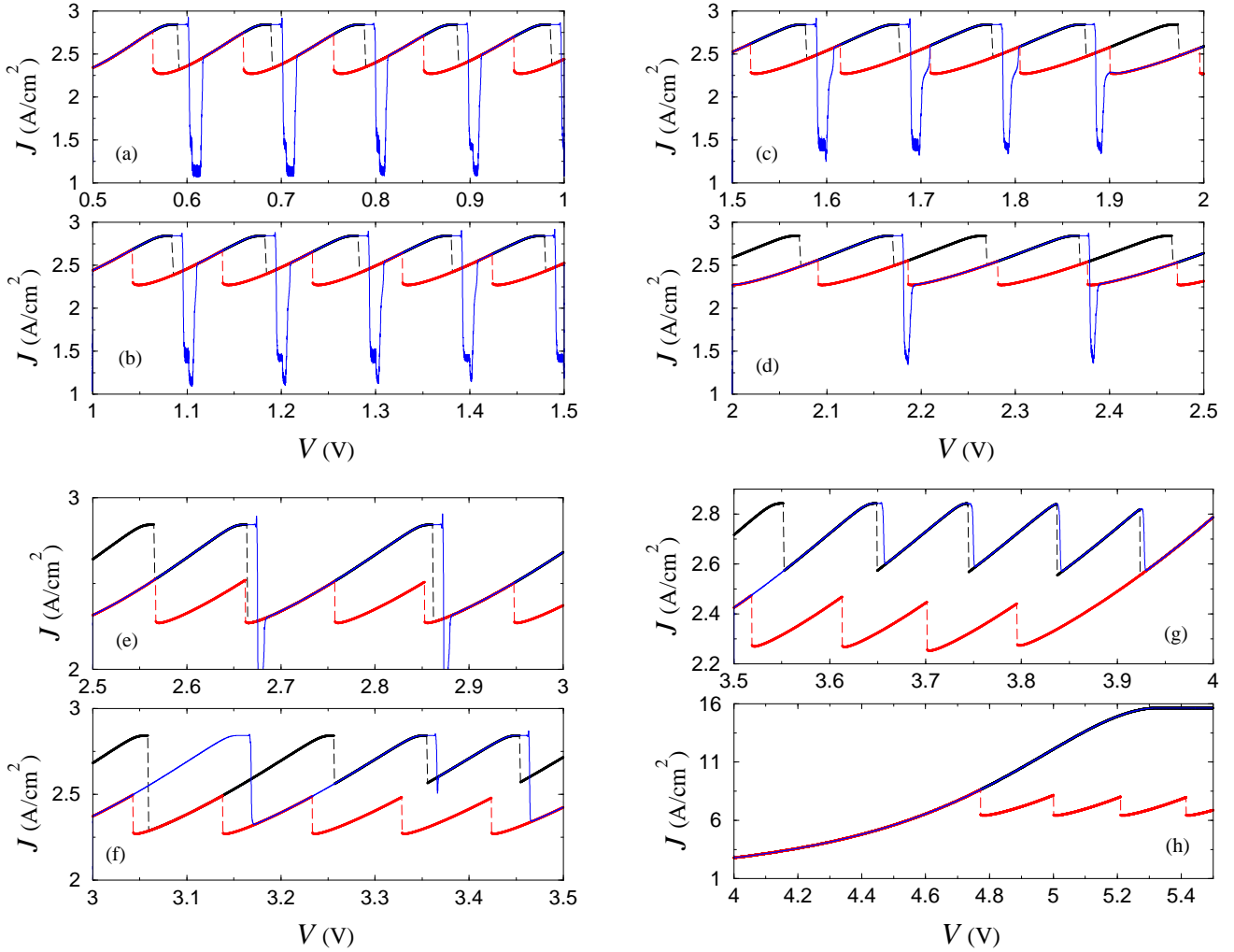


FIG. 7: (Color online) Voltage switching with $\Delta V = 0.5$ V and ramping time $\tau_r = 30 \mu\text{s}$ for different V_i on the I-V characteristics: (a) $V_i = 0.5$ V, (b) $V_i = 1$ V, (c) $V_i = 1.5$ V, (d) $V_i = 2$ V, (e) $V_i = 2.5$ V, (f) $V_i = 3$ V, (g) $V_i = 3.5$ V, (h) $V_i = 4$ V, $\Delta V = 1.5$ V. In (a), (b), (g) and (h), the current follows the I-V curve along the upper part of each branch, whereas J ranges from 6 to 16 A/cm². In (c), a branch (the 5th) is skipped for the first time. In (d) and (e), branches 3 and 5 are skipped. In (f), the upper part of the 5th branch is reached but the 6th is skipped.

VI. VOLTAGE SWITCHING TO V_f NEAR THE END OF A BRANCH

In this Section, we report the current response to voltage switching from V_i to a voltage V_f close to the end of the same branch. Firstly, we shall select branches near the end of the plateau, which were the only ones considered in Ref. [18] (see Section VI). Secondly, we shall select branches near the beginning of the plateau and observe a rather different behavior.

A. High voltages near the end of the I–V plateau

Fig. 8 depicts the current response to a voltage switching starting with a V_i in the bistable part of branch B_{37} , closer to its end. Keeping a ramping time of 100 ns, we observe similar behavior to that reported by Amann et al [18]: (i) if $V_f < V_{th}$ (the end of the static branch), the current remains on the same branch but the time it takes to settle in its final value increases as V_f approaches V_{th} ; (ii) if $V_f > V_{th}$, the final state is on the next branch, and the transient stage lasts longer as we approach V_{th} , cf. Fig. 9(a). Similarly, the longer the ramping time is, the longer the transient before the current drops to that of the following I–V branch seems to be, as indicated in Fig. 9(b). This Figure shows the influence of the ramping time on the current response to voltage switching with V_f close to V_{th} for I–V branches near the end of the plateau. We have selected now Branch B_{35} and changed the ramping time from small to large for two different V_f close to V_{th} , one larger than V_{th} , the other smaller. For $V_f > V_{th}$, we observe that the current eventually drops to the lower value on branch B_{36} , but the transient stage lasts longer as the ramping time increases. For $V_f \approx V_o < V_{th}$, the basin of attraction of B_{35} is so small that the current eventually drops to its final value on Branch B_{36} . However, the way in which this happens depends strongly on the ramping time: (i) if the ramping time is too small, the current drops rapidly and the final state on Branch B_{36} is reached soon; (ii) for intermediate ramping times, the current oscillates about the static Branch B_{35} before it falls to Branch B_{36} , and (iii) for large ramping times, the current seems to settle down to the static value on Branch B_{35} and it resists much longer before it eventually drops down to Branch B_{36} .

A distinct feature of the current response to voltage switching with V_f near the end of a static branch is that, in case (i), the final stable state for $V_f < V_{th}$ very close to V_{th} , may be oscillatory, not stationary. This is suggested by the oscillations in Figs. 8 and 9, and

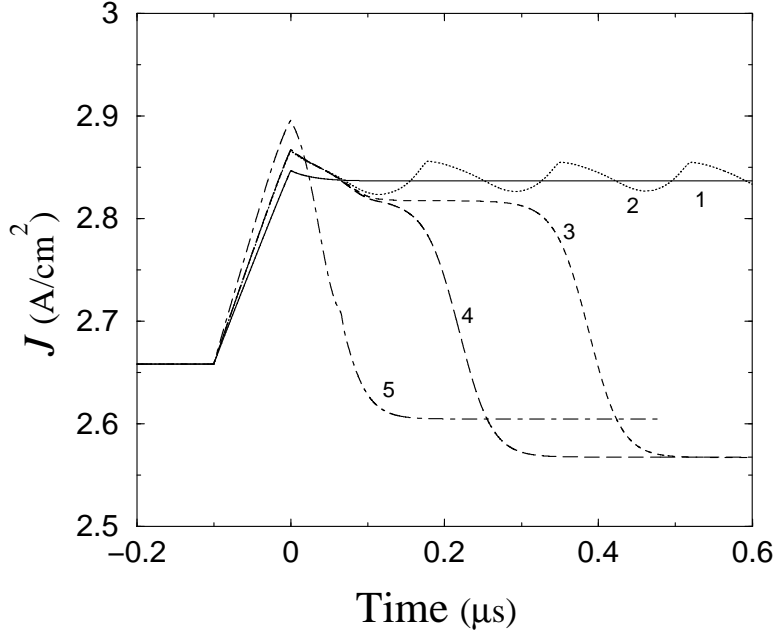


FIG. 8: Current response to voltage switching from $V_i = 3.68$ V to five different values of V_f near V_{th} (1: 3.74, 2: 3.747, 3: 3.7472732, 4: 3.7474 and 5: 3.76 V). The ramping time is $\tau_r = 100$ ns and we have set $t = 0$ at the end of voltage switching. Note the oscillatory behavior for $V_f = 3.747$ V.

further confirmed by the linear stability analysis of Appendix A. There it is shown that the static branch loses stability at some $V_o < V_{th}$ because the real part of two complex conjugate eigenvalues becomes positive for $V_o < V < V_{th}$. This is clearly seen in Fig. 10, which depicts the eigenvalues of the linear stability problem about the static branch B_{35} for 20 different voltage values close to V_{th} . For this branch, $V_o \approx 3.5547$ V.

B. Current response to switching near the end of low voltage branches

Fig. 11 shows that switching near the end of low voltage I–V branches is more complex than that described previously. It turns out that the current drop to the next branch may occur via the tripole-dipole scenario, unlike in the numerical simulations by Amann et al (who always selected high voltage static branches having intervals of tristability), but according to the experimental observations by Rogozia et al (cf. Fig. 9 of Ref. [16]). Another discrepancy between the numerical simulations of Ref. [18] and experiments is that the current spike accompanying dipole emission is much taller in the simulations (twice

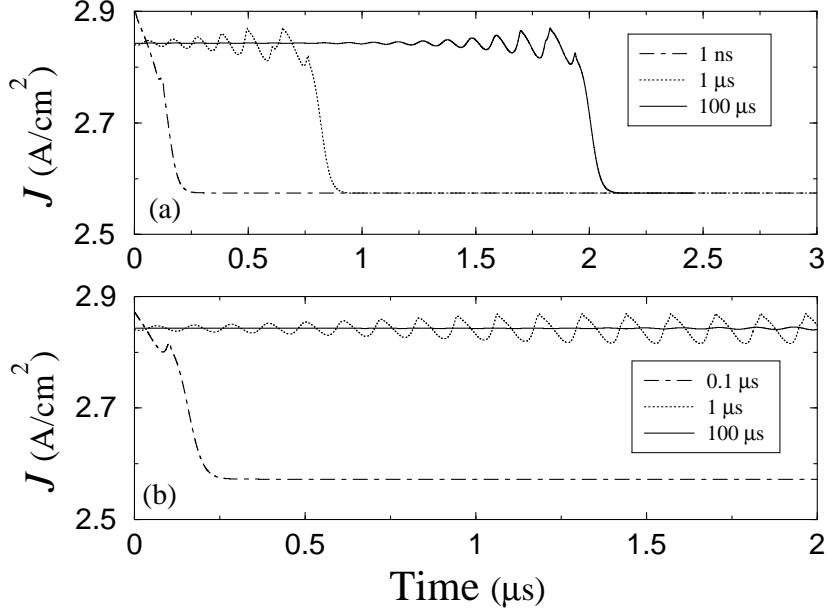


FIG. 9: Current response to voltage switching for $V_i = 3.5$ V, two different values of V_f and three different ramping times in each case: (a) $V_f = 3.555$ V $> V_{th}$, for $\tau_r = 1$ ns, 1 μ s and 100 μ s. (b) $V_f = 3.5545$ V $< V_{th}$, for $\tau_r = 0.1$ μ s, 1 μ s and 100 μ s. In all cases, we set $t = 0$ at the end of voltage switching. For $\tau_r = 100$ μ s, the current undergoes a small-amplitude oscillation in the case of Fig. 9(b).

the maximum current of the static branches instead of the experimentally observed 20% increase). In our simulations, the current spike accompanying dipole emission is much smaller than in the previous calculations by Amann et al, but this is due to the different cathode conductivity and critical current for dipole creation.

The appearance of the tripole-dipole scenario during voltage switching occurs up to voltages corresponding to branches starting to display tristability. If we fix V_f sufficiently close to V_{th} , $V_f < V_{th}$, and change the ramping time, we observe a peculiar behavior. For all ramping times, the relocation of the domain wall separating the low and high field parts of the field profile happens via the tripole-dipole scenario, as shown in Fig. 12(a). However the time t_d at which the tripole-dipole scenario starts is not a monotone function of the ramping time: it seems that t_d may have local maxima and minima as a function of τ_r . We have observed that t_d increases with τ_r up to $\tau_r \approx 2.2\mu$ s. Then t_d decreases with τ_r up to at least 7 μ s. Then t_d increases again for larger τ_r , as indicated in Fig. 12(a). We have checked that t_d is again smaller for a ramping time of 100 μ s than for $\tau_r = 30\mu$ s.

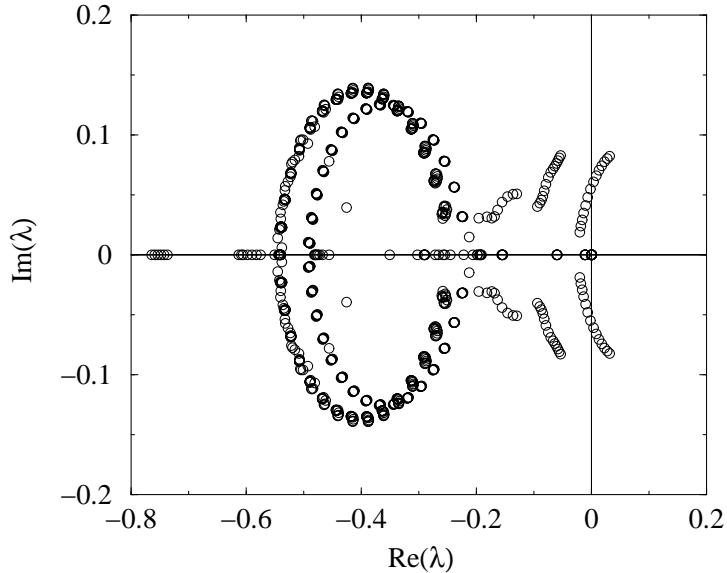


FIG. 10: Evolution of the 41 eigenvalues determining linear stability of the static branch B_{35} for 20 values of the applied voltage from $V = 3.54$ to 3.56 V.

To ascertain the origin of the non-monotonic behavior of t_d as a function of the ramping time, we observe that, as the voltage increases with time, the current becomes oscillatory before the tripole-dipole scenario begins. The shape of the current oscillations and their local period also change as the time elapses, which is clearly seen in Figs. 11 and 12(b). The latter figure also shows that, for similar ramping times, the current may drop to the lower I–V branch or continue oscillating for a longer time. Fig. 13 depicts the field profiles during the oscillations of the current shown in Fig. 12(b) for $V_f < V_{th}$. We see that the current oscillations correspond to the periodic formation of a small field pulse at the cathode and its advance towards the anode over a few SL periods before it shrinks and vanishes. Eventually as the voltage increases with time, a dipole succeeds in growing sufficiently to detach itself from the cathode region and trigger a tripole-dipole event, bringing down the current to its stable value in the next I–V branch. Fig. 14 shows that the same mechanism is responsible for similar small amplitude current oscillations for $V_f > V_{th}$.

Another clue to the different current response to switching at low voltage values is offered by linear stability analysis of the I–V static solution branches. At low voltages, they have a stationary instability at a voltage smaller than V_{th} . At that voltage, a stationary branch bifurcates and this secondary branch undergoes a Hopf bifurcation to a small amplitude

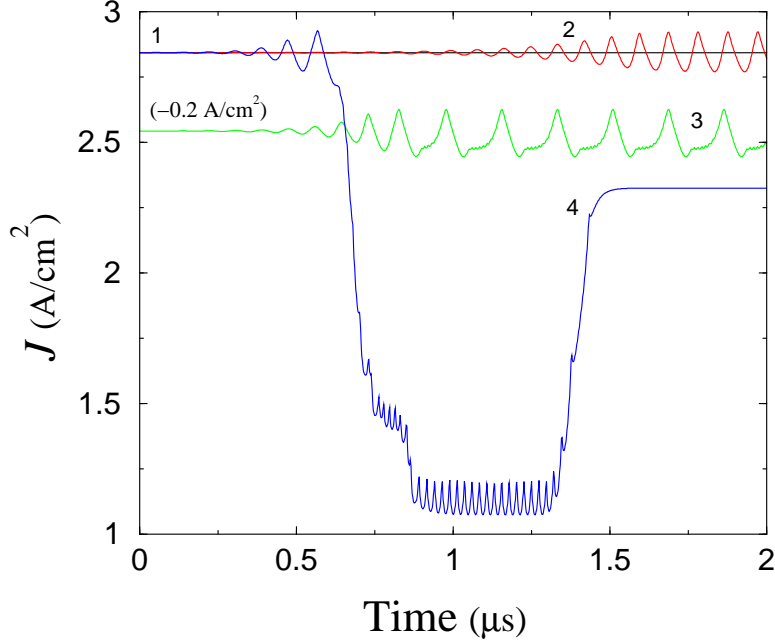


FIG. 11: (Color online) Current response to voltage switching between Branches 5 and 6 of the I–V characteristics in Fig. 2 for $V_i = 0.56$ V, ramping time $\tau_r = 10 \mu\text{s}$, and four different values of V_f near V_{th} : 1: 0.59, 2: 0.591, 3: 0.59203 and 4: 0.593 V. Note that curve 3 is shifted down 0.2 A/cm^2 for the sake of clarity.

oscillation. The field profiles for these oscillatory solution correspond to the periodic emission and motion of a small field pulse (charge dipole) confined to the region near the cathode, which is very similar to the confined Gunn effect in bulk n-GaAs and ultrapure p-Ge [23]. Figures 15(a) and (b) show that the eigenvalue determining the linear stability of the static branch B_5 is real and it vanishes at a certain voltage smaller than V_{th} . The other eigenvalues with large real parts are complex and have negative real parts. The gap in Fig. 15(b) corresponds to the oscillatory instability observed in the numerical simulations of the discrete model. It is plausible that the stationary branch that bifurcated from B_5 has a secondary oscillatory instability at that voltage, but a more detailed study is necessary before this can be ascertained. Thus we may have the following succession of bifurcations from the static branch B_5 as the voltage increases towards V_{th} : (i) stable B_5 , (ii) small amplitude static branch issuing from B_5 , (iii) Hopf bifurcation from the bifurcating static branch, (iv) annihilation of the oscillation before or at V_{th} (the end of B_5). During voltage sweeping,

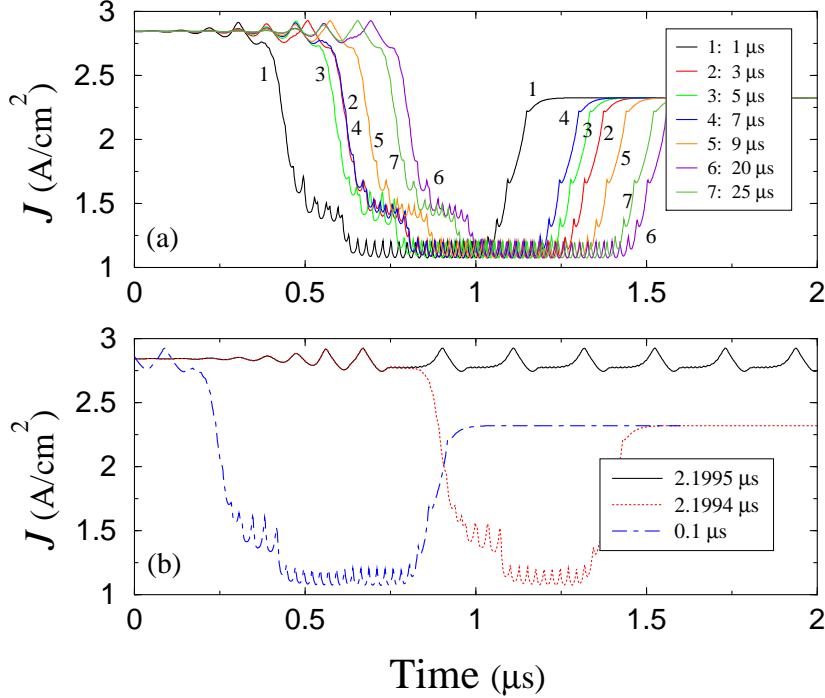


FIG. 12: (Color online) Current response to voltage switching between Branches 5 and 6 of the I-V characteristics in Fig. 2 for $V_i = 0.56 \text{ V}$. (a) $V_f = 0.593 \text{ V} > V_{th}$ and seven different ramping times from 1 to 25 μs . (b) Details of current response for $V_f = 0.59203 \text{ V} < V_{th}$ and three short ramping times: 0.1, 2.1994 and 2.1995 μs .

the current should go through this succession of bifurcations and there is no reason why the time t_d should be a monotone function of the ramping time τ_r .

VII. CONCLUSION

The relocation of the domain boundary in weakly coupled doped SL is substantially affected by the ramping time over which the voltage is switched and by multistability of the initial and final static I-V branches involved in switching. Let us consider voltage switching leaving several I-V branches between the initial and final voltages. If the ramping time is very long, the current simply follows adiabatically the change in voltage during switching, much as in up and down voltage sweeping. If the ramping time is very short, each branch jump during switching is achieved by a modified tripole-dipole scenario: a CDL is formed at the cathode, it moves towards the anode producing a second CAL behind it. Together with the old CAL, the resulting charge tripole moves towards the anode until the first CAL and

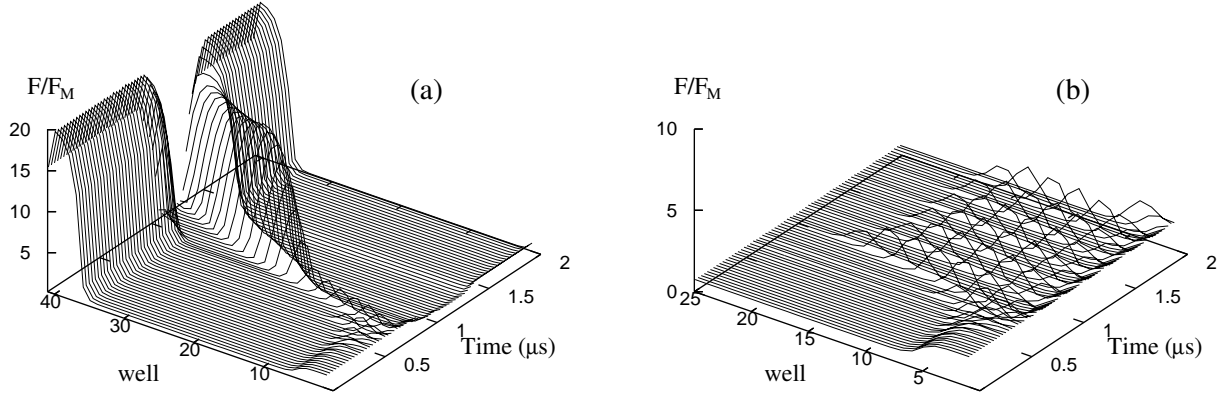


FIG. 13: Evolution of the electric field profile corresponding to Fig. 12(b), where $V_i = 0.56$ V and $V_f = 0.59203$ V $< V_{th}$, for the two (very similar) ramping times (a) $\tau_r = 2.1994$ μ s and (b) $\tau_r = 2.1995$ μ s. In (a), the CAL is emitted after a short oscillatory transient. In (b), a CAL is emitted from the cathode, it disappears in the interior of the sample and this behavior is repeated periodically. This is similar to Gunn effect oscillations confined to one part of the SL.

the CDL reach it. Then the remaining CAL moves to its final position corresponding to the new static I–V branch. For intermediate ramping time, and provided the I–V branches have wide intervals of bistability, the tripole-dipole scenario may be skipped, thereby occurring every other branch jump. If the final voltage after switching is very close to the end of a I–V branch, the current eventually drops to its value at the following static branch, but it can remain a long time on the initial static branch (or it oscillates about it in case there is an oscillatory instability) if the ramping time is sufficiently long. The time at which the tripole-dipole scenario begins and the current drops to its stable value at the next I–V branch is not a monotone function of the ramping time.

Acknowledgements

This work has been supported by the MCyT grant MAT2005-05730-C02-01. R.E. has been supported by a postdoctoral grant awarded by the Autonomous Region of Madrid.

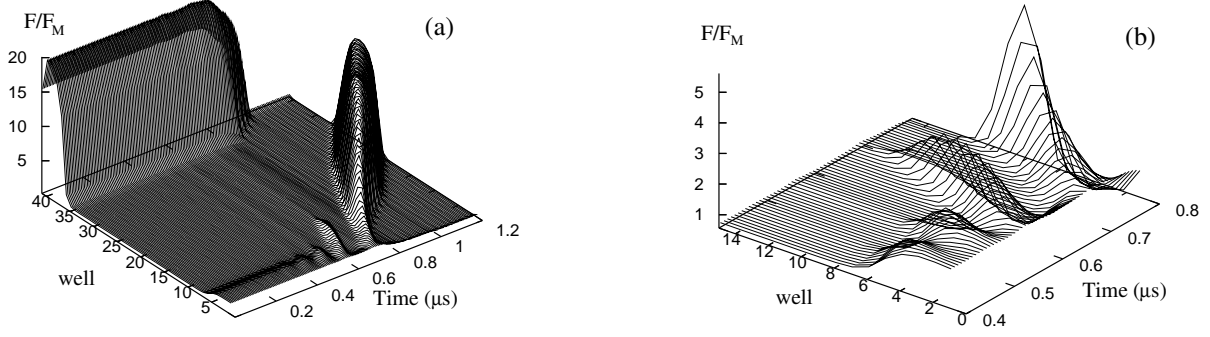


FIG. 14: Evolution of the electric field profile corresponding to curve number 6 in Fig. 12(a), which has longest oscillatory interval before a CAL is emitted from the cathode (ramping time $\tau_r = 20\mu\text{s}$). (a) Detail of the oscillatory transient regime. (b) Detail of the profile near the cathode (closest 15 wells) when the CAL is finally emitted.

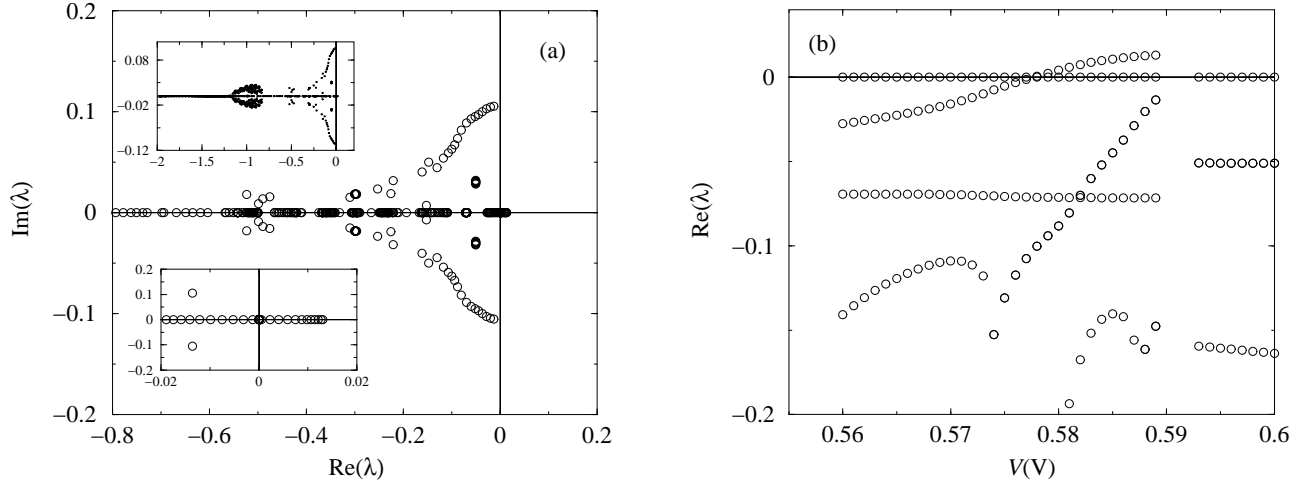


FIG. 15: (a) Evolution of the 41 eigenvalues determining linear stability of the static Branch B_5 for 20 values of the applied voltage from $V = 0.56$ to 0.6 V. The insets show the overall picture with all the eigenvalues and a zoom of the region near the imaginary axis. (b) Real part of the eigenvalues as a function of voltage. The gap in the figure corresponds to the oscillatory instability.

APPENDIX A: LINEAR STABILITY OF THE STATIC I-V BRANCHES

Let $(\{\mathcal{F}_i^*\}_{i=0}^N, \mathcal{J}^*)$ a stationary solution of (16) - (21) under dc voltage bias $\phi(\tilde{t}) \equiv \phi, \forall \tilde{t}$. In these equations, we shall eliminate the electron density in favor of the field by using the

Poisson equation. Then the tunneling current is a function of the electric field profile such that

$$\mathcal{J}_{i \rightarrow i+1}(\{\mathcal{F}_i^*\}) = \mathcal{J}^*, \quad i = 0, \dots, N, \quad (\text{A1})$$

$$\sum_{i=0}^N \mathcal{F}_i^* = (N+1)\phi. \quad (\text{A2})$$

Let $(\{f_i(\tilde{t})\}_{i=0}^N, j(\tilde{t}))$ a disturbance from the static solution:

$$\mathcal{F}_i(\tilde{t}) = \mathcal{F}_i^* + \epsilon f_i(\tilde{t}), \quad \mathcal{J}(\tilde{t}) = \mathcal{J}^* + \epsilon j(\tilde{t}). \quad (\text{A3})$$

Then, the linear equations about the static field profile and the static current density are

$$\frac{df_i}{d\tilde{t}} = j(\tilde{t}) - f_i \left. \frac{\partial \mathcal{J}_{i \rightarrow i+1}}{\partial \mathcal{F}_i} \right|_{(*)} - f_{i-1} \left. \frac{\partial \mathcal{J}_{i \rightarrow i+1}}{\partial \mathcal{F}_{i-1}} \right|_{(*)} - f_{i+1} \left. \frac{\partial \mathcal{J}_{i \rightarrow i+1}}{\partial \mathcal{F}_{i+1}} \right|_{(*)}, \quad i = 0, \dots, N, \quad (\text{A4})$$

up to $O(\epsilon)$ terms. We have set $(*) = (\mathcal{F}_i^*, \mathcal{F}_{i-1}^*, \mathcal{F}_{i+1}^*)$.

Let us now assume $f_i(\tilde{t}) = e^{\lambda \tilde{t}} f_i$, $j(\tilde{t}) = e^{\lambda \tilde{t}} j$. Then we obtain

$$\lambda f_i = j - f_i \left. \frac{\partial \mathcal{J}_{i \rightarrow i+1}}{\partial \mathcal{F}_i} \right|_{(*)} - f_{i-1} \left. \frac{\partial \mathcal{J}_{i \rightarrow i+1}}{\partial \mathcal{F}_{i-1}} \right|_{(*)} - f_{i+1} \left. \frac{\partial \mathcal{J}_{i \rightarrow i+1}}{\partial \mathcal{F}_{i+1}} \right|_{(*)}, \quad (\text{A5})$$

which can be written in matrix form as $\lambda \mathbf{f} = \mathbf{j} - \mathbf{A} \cdot \mathbf{f}$, with $a_{i,l} = \left. \frac{\partial \mathcal{J}_{i \rightarrow i+1}}{\partial \mathcal{F}_l} \right|_{(*)}$:

$$\lambda \begin{pmatrix} f_0 \\ f_1 \\ \vdots \\ f_N \end{pmatrix} = \begin{pmatrix} j \\ j \\ \vdots \\ j \end{pmatrix} - \begin{pmatrix} a_{0,0} & a_{0,1} & & & 0 \\ a_{1,0} & a_{1,1} & a_{1,2} & & \\ & a_{2,1} & a_{2,2} & & \\ & & & \ddots & a_{N-1,N} \\ 0 & & & a_{N,N-1} & a_{N,N} \end{pmatrix} \cdot \begin{pmatrix} f_0 \\ f_1 \\ \vdots \\ f_N \end{pmatrix}. \quad (\text{A6})$$

The boundary conditions for $i = 0$ and $i = N$ yield $a_{0,0} = \tilde{\sigma}$, $a_{0,1} = 0$, $a_{N,N-1} = -\tilde{\sigma} \mathcal{F}_N^* / \nu$ and $a_{N,N} = \tilde{\sigma}(\tilde{n}_N^* + \mathcal{F}_N^* / \nu)$. On the other hand, the bias condition (18) becomes

$$\sum_{i=0}^N f_i = 0. \quad (\text{A7})$$

Then $\lambda \mathbf{f} + \mathbf{A} \cdot \mathbf{f} = \mathbf{j}$ implies $\mathbf{f} = (\lambda \mathbf{I} + \mathbf{A})^{-1} \cdot \mathbf{j}$. (A7) means that the sum of the entries of the vector \mathbf{f} is zero, therefore we have

$$\sum_{i=0}^N (\lambda \mathbf{I} + \mathbf{A})^{-1} \cdot \mathbf{1} = 0, \quad (\text{A8})$$

because $j \neq 0$. The left hand side of (A8) is polynomial of degree N in λ , having therefore N zeros. For computational purposes, it is better to rewrite the system (A6)-(A7) in the form $\lambda \mathbf{f} = \mathbf{B} \cdot \mathbf{f}$. This can be achieved adding the rows in (A6) and using (A7):

$$\lambda \sum_{i=0}^N f_i = (N+1)j - (a_{0,0} + a_{1,0})f_0 - (a_{0,1} + a_{1,1} + a_{2,1})f_1 - \dots \quad (\text{A9})$$

$$\dots - (a_{i-1,i} + a_{i,i} + a_{i+1,i})f_i - \dots - (a_{N-1,N} + a_{N,N})f_N = 0. \quad (\text{A10})$$

Defining $s_i = a_{i-1,i} + a_{i,i} + a_{i+1,i}$, $i = 1, \dots, N-1$, $s_0 = a_{0,0} + a_{1,0}$ and $s_N = a_{N-1,N} + a_{N,N}$, we have

$$j = \frac{1}{N+1} \sum_{i=0}^N s_i f_i, \quad (\text{A11})$$

and therefore

$$\begin{pmatrix} j \\ j \\ \vdots \\ j \end{pmatrix} = \frac{1}{N+1} \begin{pmatrix} s_0 & s_1 & s_2 & \dots & s_N \\ s_0 & s_1 & s_2 & \dots & s_N \\ \vdots & \vdots & \vdots & & \vdots \\ s_0 & s_1 & s_2 & \dots & s_N \end{pmatrix} \cdot \begin{pmatrix} f_0 \\ f_1 \\ \vdots \\ f_N \end{pmatrix}, \quad (\text{A12})$$

which is of the form $\mathbf{j} = \frac{1}{N+1} \mathbf{S} \cdot \mathbf{f}$. Substituting this expression in (A6), we obtain a matrix equation of the type $\lambda \mathbf{f} = \mathbf{B} \cdot \mathbf{f}$, namely

$$\lambda \begin{pmatrix} f_0 \\ f_1 \\ \vdots \\ f_N \end{pmatrix} = \left\{ \frac{1}{N+1} \begin{pmatrix} s_0 & s_1 & s_2 & \dots & s_N \\ s_0 & s_1 & s_2 & \dots & s_N \\ \vdots & \vdots & \vdots & & \vdots \\ s_0 & s_1 & s_2 & \dots & s_N \end{pmatrix} - \begin{pmatrix} a_{0,0} & a_{0,1} & & & 0 \\ a_{1,0} & a_{1,1} & a_{1,2} & & \\ & & & \ddots & a_{N-1,N} \\ 0 & & & a_{N,N-1} & a_{N,N} \end{pmatrix} \right\} \cdot \begin{pmatrix} f_0 \\ f_1 \\ \vdots \\ f_N \end{pmatrix} \quad (\text{A13})$$

The matrix \mathbf{B} is equal to the matrix $\mathbf{S}/(N+1)$, except in its three main diagonals, where $b_{i,j} = s_j/(N+1) - a_{i,j}$:

$$\lambda \begin{pmatrix} f_0 \\ f_1 \\ \vdots \\ f_N \end{pmatrix} = \begin{pmatrix} b_{0,0} & b_{0,1} & b_{0,2} & \dots & b_{0,N} \\ b_{1,0} & b_{1,1} & b_{1,2} & \dots & b_{1,N} \\ \vdots & \vdots & \vdots & \ddots & \vdots \\ b_{N,0} & b_{N,1} & b_{N,2} & \dots & b_{N,N} \end{pmatrix} \cdot \begin{pmatrix} f_0 \\ f_1 \\ \vdots \\ f_N \end{pmatrix}. \quad (\text{A14})$$

The $(N+1) \times (N+1)$ matrix \mathbf{B} has a zero eigenvalue (add its rows), and its other eigenvalues are the zeros of the polynomial (A8). They have been depicted in Fig. 10.

[*] E-address bonilla@ing.uc3m.es.

- [1] A. Wacker, Phys. Rep. **357**, 1 (2002).
- [2] L. L. Bonilla, J. Phys.: Cond. Matter **14**, 341 (2002)
- [3] G. Platero and R. Aguado, Phys. Rep. **395**, 1 (2004).
- [4] L. L. Bonilla and H. T. Grahn, Rep. Prog. Phys. **68**, 577 (2005).
- [5] M. Büttiker and H. Thomas, Phys. Rev. Lett. **38**, 78 (1977).
- [6] K. Hofbeck, J. Grenzer, E. Schomburg, A. A. Ignatov, K. F. Renk, D. G. Pavel'ev, Y. Koschurinov, B. Melzer, S. Ivanov, S. Schaposchnikov, and P. S. Kop'ev, Phys. Lett. A **218**, 349 (1996).
- [7] J. Kastrup, R. Klann, H. T. Grahn, K. Ploog, L. L. Bonilla, J. Galán, M. Kindelan, M. Moscoso, and R. Merlin, Phys. Rev. B **52**, 13761 (1995).
- [8] J. Kastrup, R. Hey, K. H. Ploog, H. T. Grahn, L. L. Bonilla, M. Kindelan, M. Moscoso, A. Wacker, and J. Galán, Phys. Rev. B **55**, 2476 (1997).
- [9] D. Sánchez, M. Moscoso, L. L. Bonilla, G. Platero and R. Aguado, Phys. Rev. B **60**, 4489 (1999).
- [10] L. Esaki and L. L. Chang, Phys. Rev. Lett. **33**, 495 (1974).
- [11] Y. Kawamura, K. Wakita, H. Asahi, and K. Kurumada, Jpn. J. Appl. Phys. **25**, L928 (1986).
- [12] H. T. Grahn, K. von Klitzing, K. Ploog, and G. H. Döhler, Phys. Rev. B **43**, R12094 (1991).
- [13] G. K. Rasulova, Yu. A. Efimov and V. N. Murzin, J. Appl. Phys. **82**, 3381 (1997).
- [14] K. J. Luo, H. T. Grahn, and K. H. Ploog, Phys. Rev. B **57**, R6838 (1998).
- [15] M. Rogozia, S.W. Teitworth, H.T. Grahn, and K.H. Ploog, Phys. Rev. B **64**, 041308(R) (2001).
- [16] M. Rogozia, S.W. Teitworth, H.T. Grahn, and K.H. Ploog, Phys. Rev. B **65**, 205303 (2002).
- [17] M. Rogozia, H. T. Grahn, S. W. Teitworth and K. H. Ploog, Physica B **314**, 427 (2002).
- [18] A. Amann, A. Wacker, L. L. Bonilla, and E. Schöll, Phys. Rev. E, **63**, 066207 (2001).
- [19] L. L. Bonilla, O. Sánchez and J. Soler, Phys. Rev. B **65**, 195308 (2002).
- [20] L. L. Bonilla, in *Nonlinear Dynamics and Pattern Formation in Semiconductors and Devices*, edited by F.-J. Niedernostheide (Springer, Berlin, 1995), Chap. 1.
- [21] A. Wacker, in *Theory of Transport Properties of Semiconductor Nanostructures*, edited by E. Schöll (Chapman and Hall, London, 1998), Chap. 10.
- [22] A. Carpio, L. L. Bonilla, A. Wacker and E. Schöll, Phys. Rev. E, **61**, 4866 (2000).
- [23] L. L. Bonilla and F. J. Higuera, SIAM J. Appl. Math. **55**, 1625 (1995). I. R. Cantalapiedra, L. L. Bonilla, M. J. Bergmann and S. W. Teitworth, Phys. Rev. B **48**, 12278 (1993); see Fig. 2.